THREE-DIMENSIONAL FLOW OVER A CONICAL AFTERBODY CONTAINING A CENTERED PROPULSIVE JET: A NUMERICAL SIMULATION

GEORGE S. DEIWERT
NASA AMES RESEARCH CENTER
MOFFET FIELD, CALIFORNIA

HERBERT ROTHMUND
CONTROL DATA CORPORATION
SUNNYVALE, CALIFORNIA

THREE-DIMENSIONAL FLOW OVER A CONICAL AFTERBODY CONTAINING A CENTERED PROPULSIVE JET: A NUMERICAL SIMULATION

George S. Deiwert*
NASA Ames Research Center, Moffett Field, California

Herbert Rothmund†
Control Data Corporation, Sunnyvale, California

Abstract

The supersonic flow field over a body of revolution incident to the free stream is simulated numerically on a large, array processor (the CDC Cyber 205). The configuration is composed of a cone-cylinder forebody followed by a conical afterbody from which emanates a centered, supersonic propulsive jet. The free-stream Mach number is 2, the jet-exit Mach number is 2.5, and the jet-to-free-stream static pressure ratio is 3. Both the external flow and the exhaust are ideal air at a common total temperature. The thin-layer approximation to the time-dependent, compressible, Reynolds-averaged Navier-Stokes equations are solved using an implicit finite-difference algorithm. The data base, of 5 million words, is structured in a "pencil" format so that efficient use of the array processor can be realized. The computer code is completely vectorized to take advantage of the data structure. Turbulence closure is acheived using an empirical algebraic eddy-viscosity model. The configuration and flow conditions correspond to published experimental tests and the computed solutions are consistent with the experimental data.

Introduction

In 1980, a computational study was described in which the three-dimensional flow field over axisymmetric boattailed bodies at moderate angles of attack was simulated.[1] The exhaust plumes were modeled by solid plume simulators, and a second-order-accurate, implicit finite-difference algorithm was used to solve the governing partial differential equations on the ILLIAC IV array processor. Several flow fields were computed and the results compared with published experimental data. The promising results of that first study provided the incentive to extend the work to include propulsive exhaust jets emanating from the afterbody base. The ILLIAC IV was subsequently removed from service, however, and it became necessary to scale down the size and scope of the study to the capacity of existing computer resources.

*Research Scientist, Member AIAA.
†Computer Analyst.

In January 1983, the results of a study of supersonic axisymmetric flow over boattails containing a centered propulsive jet were presented.[2] Those results, obtained using a Cray 1S computer with 10^6 words of main memory, were compared with existing experimental data. Jet-to-free-stream static pressure ratio and nozzle exit angle were varied parametrically; and the predicted trends agreed well with experiment.

The purpose of this paper is to describe the vectorized implementation of the three-dimensional Navier-Stokes code on a Cyber 205 computer for boattailed afterbodies at moderate angles of attack that contain a centered propulsive jet. Some computed results, which correspond in part to a published experimental study for a like configuration and flow conditions, are included for illustration.

Afterbody Configuration

The geometric configuration is a 9 caliber body of revolution composed of a 14° half-angle conical nose, a cylindrical forebody, and an 8° half-angle conical afterbody of 1 caliber length. Centered inside the afterbody is a conical nozzle with exit diameter of 0.6 caliber that is flush with the afterbody base. The nozzle exit half-angle is 20°.

Experimental studies for the same configuration were performed by White and Agrell[3] for the model immersed in an air stream flowing at $M_\infty = 2.0$ and a jet-exit Mach number of 2.5. White and Agrell considered angles of incidence to the free stream up to 8° and jet-to-free-stream static-pressure ratios up to 15. Because of limited acces to the Cyber 205 computer, computed results are included in this paper only for the case in which the angle of incidence is 6° and the jet-to-free-stream pressure ratio is 3.0.

Governing Equations

The equations describing the flow are the Reynolds-averaged Navier-Stokes equations. These are written below in strong conservative form in generalized coordinates as

$$\partial_t Q + \partial_\xi(F \cdot \vec{g}^\xi) + \partial_\eta(F \cdot \vec{g}^\eta) + \partial_\zeta(F \cdot \vec{g}^\zeta) = 0 \quad (1)$$

where

$$Q = J^{-1}\begin{pmatrix} \rho \\ \rho u \\ \rho v \\ \rho w \\ e \end{pmatrix}, \quad F = J^{-1}\begin{pmatrix} \rho\vec{q} \\ \rho u\vec{q} + \tau\cdot\vec{e}_x \\ \rho v\vec{q} + \tau\cdot\vec{e}_y \\ \rho w\vec{q} + \tau\cdot\vec{e}_z \\ e\vec{q} + \tau\cdot\vec{q} - K_e\nabla T \end{pmatrix}$$

and $\vec{e}_x, \vec{e}_y$, and $\vec{e}_z$ are the Cartesian unit vectors and $\vec{g}^{\xi}, \vec{g}^{\eta}$, and $\vec{g}^{\zeta}$ are the contravariant base vectors, which can be written as

$$\vec{g}^{\xi} = \xi_x\vec{e}_x + \xi_y\vec{e}_y + \xi_z\vec{e}_z$$
$$\vec{g}^{\eta} = \eta_x\vec{e}_x + \eta_y\vec{e}_y + \eta_z\vec{e}_z$$
$$\vec{g}^{\zeta} = \zeta_x\vec{e}_x + \zeta_y\vec{e}_y + \zeta_z\vec{e}_z$$

The components of momentum, $\rho u, \rho v$, and ρw, are in Cartesian space and the velocity vector $\vec{q}$ is generally expressed in terms of the contravariant velocity components, U, V, and W as

$$\vec{q} = u\vec{e}_x + v\vec{e}_y + w\vec{e}_z$$
$$= U\vec{g}_{\xi} + V\vec{g}_{\eta} + W\vec{g}_{\zeta}$$

where $\vec{g}_{\xi}, \vec{g}_{\eta}$, and $\vec{g}_{\zeta}$ are the covariant base vectors written as

$$\vec{g}_{\xi} = x_{\xi}\vec{e}_x + y_{\xi}\vec{e}_y + z_{\xi}\vec{e}_z$$
$$\vec{g}_{\eta} = x_{\eta}\vec{e}_x + y_{\eta}\vec{e}_y + z_{\eta}\vec{e}_z$$
$$\vec{g}_{\zeta} = x_{\zeta}\vec{e}_x + y_{\zeta}\vec{e}_y + z_{\zeta}\vec{e}_z$$

The Jacobian J of the transformation is given by

$$J^{-1} = x_{\xi}y_{\eta}z_{\zeta} + x_{\zeta}y_{\xi}z_{\eta} + x_{\eta}y_{\zeta}z_{\xi}$$
$$- x_{\xi}y_{\zeta}z_{\eta} - x_{\eta}y_{\xi}z_{\zeta} - x_{\zeta}y_{\eta}z_{\xi}$$

The flux vector F can be decomposed into a parabolic part, F_P, which contains only gradient diffusive terms, and a hyperbolic part, F_H, which contains only convective-like terms, as

$$F_H = \begin{pmatrix} \rho\vec{q} \\ \rho u\vec{q} + p\vec{e}_x \\ \rho v\vec{q} + p\vec{e}_y \\ \rho w\vec{q} + p\vec{e}_z \\ (e+p)\vec{q} \end{pmatrix}, \quad F_P = F - F_H \quad (2)$$

For flows in which the shear layers are thin (when $Re >> 1$) and aligned with one principal plane (say the plane normal to the η coordinate), the parabolic part of F can be neglected in the other two coordinates (ξ and ζ), without any real loss in accuracy. This is consistent with boundary-layer theory and yet maintains the coupling between the viscous and inviscid regions that is critical in simulating interactive flows. With this thin-layer approximation, Eq. (1) is rewritten as:

$$\partial_t Q + \partial_{\xi}(F_H\cdot\vec{g}^{\xi}) + \partial_{\eta}(F\cdot\vec{g}^{\eta}) + \partial_{\zeta}(F_H\cdot\vec{g}^{\zeta}) = 0 \quad (3)$$

Computational Grid

A body-oriented computational grid is constructed in a manner compatible with the thin-layer approximation. Shown in Fig. 1 is the grid used in the present computations. Figure 1a shows the complete configuration and Fig. 1b the detail in the base region of the afterbody. Radial grid lines on the forebody join the surface orthogonally. On the afterbody and in the exhaust plume, the radial lines are normal to the body axis. There are 81 points distributed along the body,

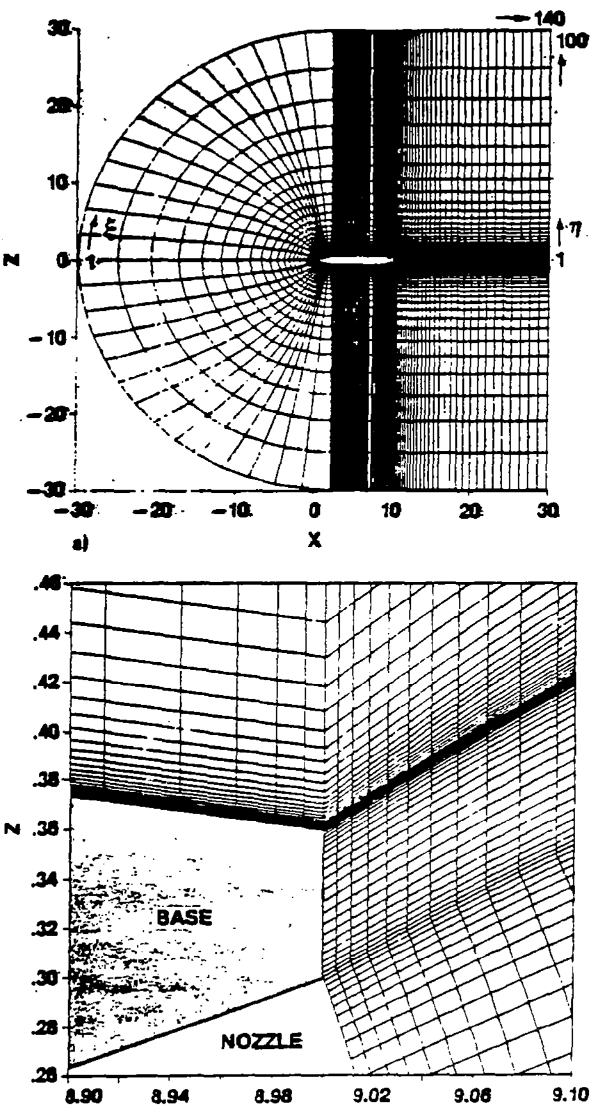

Fig. 1 Computational grid: bilateral plane of symmetry. a) Complete configuration (140 x 100 x 20); b) Base-region detail.

with clustering near the nose and near the base. Of the 81 points, 21 are used to define the afterbody shape; the afterbody is 1 caliber long. An additional 59 points are distributed downstream of the afterbody to a distance equal to 21 forebody diameters from the nozzle base. These 140 total points define the ξ coordinate distribution. The radial distribution, corresponding to the η coordinate, extends from the body surface to a distance equal to 30 forebody diameters both ahead of the nose and normal to the body axis. A total of 60 points is used in this region, with a high degree of streching used in order to resolve the sublayer of the turbulent boundary layer. (Here the first grid point off the body surface corresponds approximately to a value of η^+ of 8 where $\eta^+ = (\rho_w \tau_w)^{1/2}(\eta - \eta_w)/\mu_w$.) An additional 40 points are distributed across the nozzle and its blunt base, extending from the centerline to the body surface. Of these, 20 are in the jet exit plane and 20 are on the blunt base itself.

One- and two-parameter hyperbolic-tangent streching functions[4] are used in the base region to focus resolution near the corners and to achieve a smooth, piecewise continuous distribution of points across the exhaust plume and base. At the nozzle exit, points are distributed along an arc describing the conical flow exit plane (that is, the arc radius is equal to the nozzle exit radius of 0.3 caliber divided by the sine of the nozzle-exit half-angle of 20°). Downstream of the nozzle, the grid lines are aligned so as to closely approximate the exhaust plume shape for an experimentally observed axisymmetric flow by Agrell and White,[5] which is for the same geometric configuration and free-stream conditions, but for a jet-to-free-stream pressure ratio of 9. The third dimension, ζ, is generated by rotating the two-dimensional (ξ, η) grid about the cylindrical axis while maintaining a uniform angular distribution between the rotated planes. Here, 20 radial planes are used with planes 2 and 19 coinciding with the bilateral plane of symmetry, where plane 2 corresponds to the lee and plane 19 to the windward. Planes 1 and 20 are image planes used to enforce a symmetry boundary condition. Thus, there are (ξ, η) planes distributed every 10.588° around the half-body.

The total grid dimensions are (140 x 100 x 20), corresponding to the ξ, η, and ζ directions, respectively, for a total of 280,000 points. Of these, (80 x 40 x 20), or 64,000, lie inside the body and are not used in the computation, leaving an actual total of 216,000 points used in the computation.

Data Structure

There are 23 variables required at each grid point corresponding to the 5 conserved quantities in the Q vector, 5 residuals for the solution vector, 9 metric coefficients, the Jacobian of the transformation, and 3 components of vorticity used in the turbulence transport model. This results, for a computational grid of 216,000 points, in a data base of 5 x 10^6 words.

To accommodate this large data base on a vector processor with a limited main memory, the computational grid is divided into subsets called "blocks." This data structure was originally devised for implementation on the ILLIAC IV array processor by Lomax and Pulliam and is described in detail in Ref. 6. In the present case, each block is a 20 x 20 x 20 cube for a total of 8,000 points and a data base subset of 184,000 words for the 23 variables. The blocks are stacked together in each coordinate direction to form a sequence of blocks called "pencils."

For a given coordinate direction, one complete pencil of data is loaded into the central memory, and computations are performed on that data corresponding to the coordinate direction. At any point in the computation, only 17 variables are required to be in the main memory at one time (6 of the 9 metric coefficients are not used in any given direction). This results in a data-base subset of 136,000 words. For a processor with 10^6 words of main memory then, as many as seven blocks of data can be held in storage for immediate processing. The block dimension is an adjustable parameter and is limited only by the maximum pencil length and the main memory of the vector processor.

Shown in Fig. 2, in physical coordinates, are the block boundaries for the present configuration. Figure 2a shows the complete configuration and Fig. 2b the detail in the afterbody region. Figure 3 shows the corresponding block structure in computational space. The mesh nodes of the computational domain are arranged in a rectangular latice with positive integer coordinates (ξ, η, ζ). Each node belongs to three pencils, a ξ-pencil, an η-pencil, and a ζ-pencil. The pencils of each sweep direction are given a definite order. For the ξ-pencils, the η-coordinate varies most rapidly as the pencil index increases; for both the η-pencils and ζ-pencils the coordinate ξ varies most rapidly. Figure 4 illustrates this sequencing for the present data structure.

Within a pencil, the planes are naturally ordered by the sweep coordinate. The pencils of data can be stored in the correct pencil ordering for just one sweep direction only. When sweeping in the other directions, pencils of data are gathered and fetched for computation and scattered back when writing the updated values. Additionally, the ordering of nodes within a plane can be correct for just one sweep direction, and it is necessary to transpose the the data in memory so that each plane of nodes normal to the sweep direction forms a contiguous set of memory locations. In the present code, the ordering of nodes is correct for the ξ-direction and transpose routines are used for the other sweep directions.

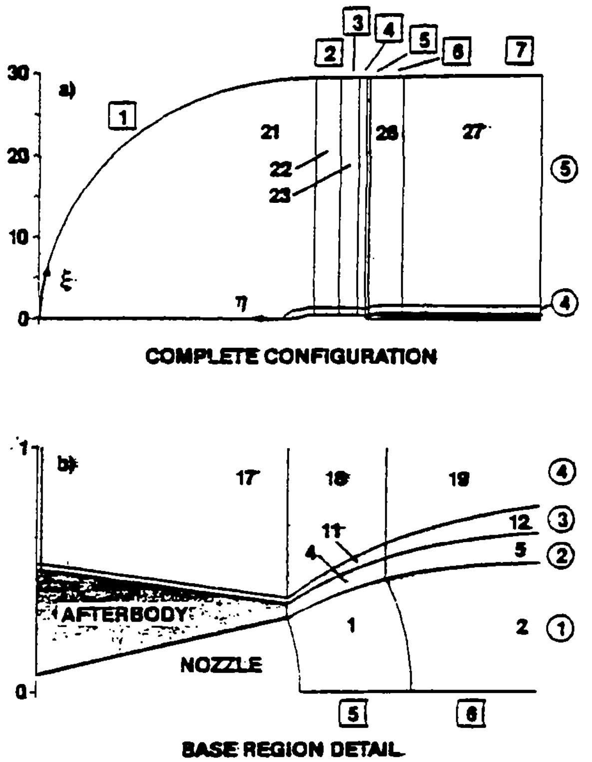

Fig. 2 Block boundaries: physical space. a) Complete configuration; b) Base-region detail.

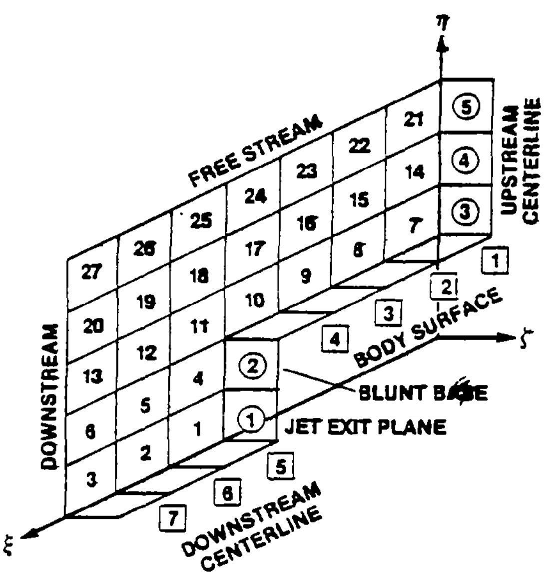

Fig. 3 Block boundaries: computational space, complete configuration.

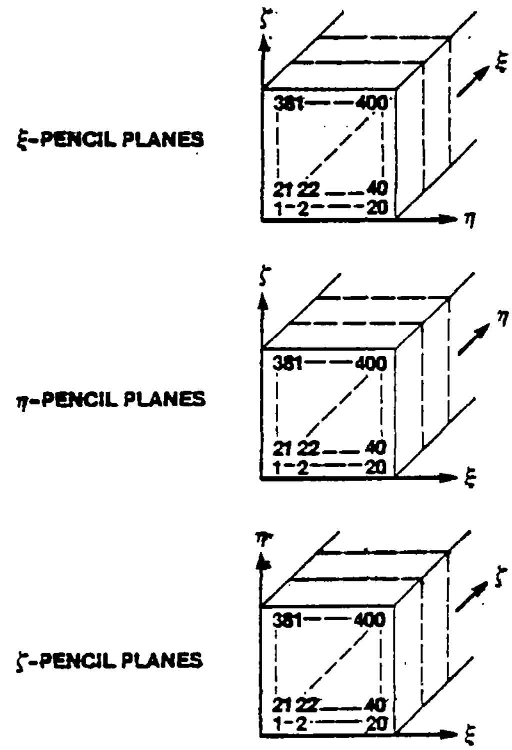

Fig. 4 Data structure within pencil data base.

Numerical Algorithm

The numerical algorithm used to solve Eq. (3) is the approximate factored scheme of Beam and Warming.[7] Rewriting Eq. (3) as

$$\partial_t Q = -\partial_\xi(F_H\cdot\vec{g}^{\xi}) - \partial_\eta(F\cdot\vec{g}^{\eta}) - \partial_\zeta(F_H\cdot\vec{g}^{\zeta}) = \mathcal{R} \quad (4)$$

the corresponding difference equation is then

$$\mathcal{L}_\eta \mathcal{L}_\zeta \mathcal{L}_\xi \Delta_t Q = \mathcal{R}_\xi + \mathcal{R}_\eta + \mathcal{R}_\zeta \quad (5)$$

where the operators are defined by

$$\begin{aligned}
\mathcal{L}_\xi &= \left(I + \Delta t\,\delta_\xi A^n - \epsilon_I J^{-1}\nabla_\xi\Delta_\xi J\right)\\
\mathcal{L}_\eta &= \left(I + \Delta t\,\delta_\eta C^n - \epsilon_I J^{-1}\nabla_\eta\Delta_\eta J - \Delta t\,\delta_\eta J^{-1} M^n J\right)\\
\mathcal{L}_\zeta &= \left(I + \Delta t\,\delta_\zeta B^n - \epsilon_I J^{-1}\nabla_\zeta\Delta_\zeta J\right)\\
\mathcal{R}_\xi &= -\Delta t\,\delta_\xi\left(JF_H\cdot\vec{g}^{\xi}\right)^n - \epsilon_E J^{-1}(\nabla_\xi\Delta_\xi)^2 J\,Q^n\\
\mathcal{R}_\eta &= -\Delta t\,\delta_\eta\left(JF\cdot\vec{g}^{\eta}\right)^n - \epsilon_E J^{-1}(\nabla_\eta\Delta_\eta)^2 J\,Q^n\\
\mathcal{R}_\zeta &= -\Delta t\,\delta_\zeta\left(JF_H\cdot\vec{g}^{\zeta}\right)^n - \epsilon_E J^{-1}(\nabla_\zeta\Delta_\zeta)^2 J\,Q^n
\end{aligned}$$

where the δ_ξ, δ_η, and δ_ζ are central-difference operators; ∇_ξ, ∇_η, and ∇_ζ are backward-difference operators; and Δ_ξ, Δ_η, and Δ_ζ are forward-difference operators in the ξ-, η-, and ζ-directions, respectively. The Δ_t term is a forward-difference operator in time. For example,

$$\Delta_t Q = Q^{n+1} - Q^n$$

$$\Delta_\xi Q = Q(\xi + \Delta\xi, \eta, \varsigma) - Q(\xi, \eta, \varsigma)$$

and

$$\nabla_\xi Q = Q(\xi, \eta, \varsigma) - Q(\xi - \Delta\xi, \eta, \varsigma)$$

The Jacobian matrices

$$A = \partial_Q (F_H \cdot \vec{g}^\xi)$$

$$B = \partial_Q (F_H \cdot \vec{g}^\eta)$$

$$C = \partial_Q (F_H \cdot \vec{g}^\varsigma)$$

$$M = \partial_Q (F_P \cdot \vec{g}^\eta)$$

are described in detail by Pulliam and Steger.[8] Fourth-order explicit terms (preceded by the coefficient ϵ_E) and second-order implicit terms (preceded by the coefficient ϵ_I) have been added to control nonlinear instabilities.

Equation (5) is solved in three successive sweeps of the data base, each sweep inverting one of the operators on the left-hand side:

$$\mathcal{L}_\varsigma \mathcal{L}_\xi \Delta_t Q = \mathcal{L}_\eta^{-1} (\mathcal{R}_\xi + \mathcal{R}_\eta + \mathcal{R}_\varsigma)$$

$$\mathcal{L}_\xi \Delta_t Q = \mathcal{L}_\varsigma^{-1} \mathcal{L}_\eta^{-1} (\mathcal{R}_\xi + \mathcal{R}_\eta + \mathcal{R}_\varsigma)$$

$$\Delta_t Q = \mathcal{L}_\xi^{-1} \mathcal{L}_\varsigma^{-1} \mathcal{L}_\eta^{-1} (\mathcal{R}_\xi + \mathcal{R}_\eta + \mathcal{R}_\varsigma)$$

The solution is advanced in time by adding $\Delta_t Q$ to Q after the ξ sweep.

In the general case, pencils of data are loaded into central memory four times and operated on for each time-step advance: once each for the ξ and η directions and twice for the ς direction. First the right-hand side of Eq. (5) is formed and then the left-hand-side operators are inverted one by one. A flow schematic showing the ordering of operations, including data reads, transposes, computations, and data writes is shown below where the symbols R and ω represent variables used to accumulate the right-hand-side elements and vorticity elements, respectively, for each coordinate direction.

ξ-pencils: (initial step only)

Read:	Q, J, ξ-metrics
Compute:	$\mathrm{R} = \mathcal{R}_\xi$, $\omega = \omega(\xi)$
Write:	R, ω

<u>Begin Loop</u>

ς-pencils:

Read:	Q, J, R, ω, ς-metrics
Transpose:	Q, J, R, ω
Compute:	$\mathrm{R} = \mathcal{R}_\xi + \mathcal{R}_\varsigma$,
	$\omega = \omega(\xi) + \omega(\varsigma)$
Transpose:	R, ω
Write:	R, ω

η-pencils:

Read:	Q, J, R, ω, η-metrics
Transpose:	Q, J, R, ω
Compute:	$\omega = \omega(\xi) + \omega(\varsigma) + \omega(\eta)$
	$\mu_T(\omega)$
	$\mathrm{R} = \mathcal{R}_\xi + \mathcal{R}_\varsigma + \mathcal{R}_\eta$
	$\mathcal{L}_\eta^{-1}(\mathrm{R})$
Transpose:	$\mathcal{L}_\eta^{-1}(\mathrm{R})$
Write:	$\mathcal{L}_\eta^{-1}(\mathrm{R})$

ς-pencils:

Read:	Q, J, $\mathcal{L}_\eta^{-1}(\mathrm{R})$, ς-metrics
Transpose:	Q, J, $\mathcal{L}_\eta^{-1}(\mathrm{R})$
Compute:	$\mathcal{L}_\varsigma^{-1}\mathcal{L}_\eta^{-1}(\mathrm{R})$
Transpose:	$\mathcal{L}_\varsigma^{-1}\mathcal{L}_\eta^{-1}(\mathrm{R})$
Write:	$\mathcal{L}_\varsigma^{-1}\mathcal{L}_\eta^{-1}(\mathrm{R})$

ξ-pencils:

Read:	Q, J, $\mathcal{L}_\varsigma^{-1}\mathcal{L}_\eta^{-1}(\mathrm{R})$, ξ-metrics
Compute:	$\Delta_t Q$, Q, $\mathrm{R} = \mathcal{R}_\xi$, $\omega = \omega(\xi)$
Write:	Q, R, ω

<u>End Loop</u>

In this flow sequence, 62 variables are read, 57 variables are transposed, and 31 variables are written. For the special case in the present study in which the ς-pencils are just one block long, a more efficient operation sequence can be used that substantially reduces the number of reads and writes required. This is shown below.

ξ-pencils: (initial step only)

Read:	Q, J, ξ-metrics
Compute:	$\mathrm{R} = \mathcal{R}_\xi$, $\omega = \omega(\xi)$

<u>Begin Loop</u>

ς-pencils:

Read:	ς-metrics
Transpose:	Q, J, R, ω
Compute:	$\mathrm{R} = \mathcal{R}_\xi + \mathcal{R}_\varsigma$
	$\omega = \omega(\xi) + \omega(\varsigma)$
Transpose:	R, ω
Write:	R, ω

η-pencils:

Read:	Q, J, R, ω, η-metrics
Transpose:	Q, J, R, ω
Compute:	$\omega = \omega(\xi) + \omega(\varsigma) + \omega(\eta)$
	$\mu_T(\omega)$
	$\mathrm{R} = \mathcal{R}_\xi + \mathcal{R}_\varsigma + \mathcal{R}_\eta$
	$\mathcal{L}_\eta^{-1}(\mathrm{R})$

ς-pencils:

Read:	ς-metrics
Transpose:	Q, J, $\mathcal{L}_\eta^{-1}(\mathrm{R})$
Compute:	$\mathcal{L}_\varsigma^{-1}\mathcal{L}_\eta^{-1}(\mathrm{R})$
Transpose:	$\mathcal{L}_\varsigma^{-1}\mathcal{L}_\eta^{-1}(\mathrm{R})$
Write:	$\mathcal{L}_\varsigma^{-1}\mathcal{L}_\eta^{-1}(\mathrm{R})$

ξ-pencils:

Read:	Q, J, $\mathcal{L}_\varsigma^{-1}\mathcal{L}_\eta^{-1}(\mathrm{R})$, ξ-metrics
Compute:	$\Delta_t Q$, Q
	$\mathrm{R} = \mathcal{R}_\xi$, $\omega = \omega(\xi)$
Write:	Q,

<u>End Loop</u>

In this flow sequence, 32 variables are read, 52 are transposed, and 18 variables are written, a savings of nearly 50% in the I/O. In both the general case and the special case, the data read-transpose sequence and the transpose-write sequence can be replaced by the more efficient "gather" and "scatter" commands available for the Cyber 205 (Ref. 9). Further improvements in efficiency can be obtained by using asynchronous I/O in conjunction with a rotating memory backing store. The most efficient code, however, will be realized by using a solid-state backing store in conjunction with gather and scatter commands or with a code that is fully core contained.

The numerical algorithm conforms well to large vectorization. For block sizes of 20 x 20 x 20, the vector length is 400. Timing studies with the present code indicate an MFLOP rate (million of floating- point operations per second) of 115 when computing in half precision (32-bit word lengths) on a 2-pipe configuration. On a 4-pipe configuration the MFLOP rate increased to 207. There are approximately 3,800 floating point operations executed for every grid node per time step resulting in a CPU time of 33 x 10^{-6} sec per point per time-step on a 2-pipe machine and 18 x 10^{-6} sec per point per time-step on a 4-pipe machine. The transpose times (transposes do not contain any floating-point operations) are 5.6 x 10^{-6} sec per point. Equivalent transposes performed by gather and scatter instructions require just 1.8 x 10^{-6} sec per point. When synchronized I/O to and from rotating backing store was used, the average I/O time was 25 msec per variable per block. This translates directly into 172 x 10^{-6} sec per point, but overlapping the I/O reduces this to 94 x 10^{-6} sec per point. (The Cyber 205 used for these timing studies was configured with four I/O channels to accommodate overlapping.) This time, a result in large part of the latency time in accessing disk files, can be reduced to nearly zero by using I/O buffers in conjunction with asynchronous I/O or with solid-state backing storage. The use of I/O buffers, however, implies the availability of additional main memory and imposes an additional constraint on the pencil size. To avoid this constraint, the data flow should be modified such that a subset of contiguous blocks of data in a pencil are operated on while blocks at each end of the subset are being buffered in and out.

Boundary Conditions

Boundary conditions are imposed at the ends of each data pencil; the data pencils are identified by number in Fig. 3. For the ξ-direction, pencil No. 1 starts at the jet-exit plane. Supersonic conical flow conditions corresponding to a jet-exit Mach number of 2.5 and a static pressure of $3p_\infty$ are imposed at the first data plane. At the last plane of each of the five ξ-pencils, which correspond to the outflow boundary, first-order extrapolation is used so that $\partial_\xi Q = 0$. Pencil No. 2 in the ξ-direction begins at the blunt base. Here slip conditions and an impermeable adiabatic wall are imposed so that

$$\partial_\xi(\rho) = \partial_\xi(\rho v) = \partial_\xi(\rho w) = 0$$

$$\rho u = 0$$

$$\partial_\xi[e - 0.5(\rho u^2 + \rho v^2 + \rho w^2)] = 0$$

Pencils 3, 4, and 5 in the ξ-direction begin on the grid centerline of revolution (at $\xi = 0$) ahead of the forebody nose. Here a second order extrapolation to the centerline is used such that

$$\partial_\xi(\rho) = \partial_\xi(\rho u) = \partial_\xi(\rho w) = \partial_\xi(\rho e) = 0$$

while the lateral momentum is set to zero

$$\rho v = 0$$

In addition, at each η, the Q values are averaged over ζ on the centerline and used as boundary values for all ζ at each η. Special treatment of the base corner at the afterbody–blunt-base junction is used to account for the singular nature of that line. For the ξ-sweeps, the ζ-line of data in pencil No. 3 that corresponds to this corner is treated in the same manner as the first plane of data in pencil No. 2 that corresponds to the blunt base. This line of data is treated differently in the η-sweep and is described in the second paragraph following.

After the forebody flow field is fully developed during the course of the solution, the first two η-pencils can be dropped from the computation and boundary conditions imposed on the ξ-pencils that correspond to the fully developed flow at the plane that is the upstream boundary of η-pencil No. 3. This reduces the total data base by six blocks without altering the validity of the solution. This simplification is strictly valid only for supersonic external flows. The solution downstream can be further developed to steady state, and jet parameters can even be varied to generate additional solutions.

Boundary conditions for the η-direction consist of the imposition of free stream conditions at the last plane of each of the seven η-pencils; no-slip, adiabatic wall condition for the first plane of η-pencils 1 through 4, which correspond to the body surface; and first-order extrapolation to the centerline for pencils 5, 6, and 7 such that $\partial_\eta Q = 0$. Centerline averaging, as described for the ξ-pencil boundary ahead of the body, is also used for the η-pencil boundary in the jet. The line of data in η-pencil No. 5, which corresponds to the corner between the afterbody and the blunt base, is treated in the same manner as the first plane of η-pencils 1 through 4. As a result, this line of data is double valued: one value for the ξ sweep described previously and the no-slip, adiabatic value for the η-sweep.

For the ζ-direction, bilateral symmetry is imposed by setting the data at the first and last ζ-planes equal to the values in the third plane and in the second from last plane, respectively, with a sign change included in the lateral momentum component (ρv).

Turbulence Closure

The Reynolds stresses and turbulent heat-flux terms have been included in the stress tensor and heat-flux vector by using the eddy-viscosity and eddy-conductivity concept, whereby the coefficients of viscosity and thermal conductivity are the sum of the molecular (laminar) part and an eddy (turbulent) part. Eddy-viscosity models incorporate turbulent transport into the molecular-transport stress tensor by adding the scalar eddy-viscosity transport coefficient μ_T to the coefficient of molecular viscosity, ($\mu_e = \mu + \mu_T$), thereby relating turbulent transport directly to gradients of the mean-flow variables. In a Cartesian coordinate system, the three-dimensional molecular stress tensor can be written as

$$\begin{aligned}\tau_\ell = &(p+\sigma_x)\vec{e}_x\vec{e}_x + \tau_{xy}\vec{e}_x\vec{e}_y + \tau_{xz}\vec{e}_x\vec{e}_z \\ &\tau_{yx}\vec{e}_y\vec{e}_x + (p+\sigma_y)\vec{e}_y\vec{e}_y + \tau_{yz}\vec{e}_y\vec{e}_z \\ &\tau_{zx}\vec{e}_z\vec{e}_x + \tau_{zy}\vec{e}_z\vec{e}_y + (p+\sigma_z)\vec{e}_z\vec{e}_z\end{aligned}$$

In the thin-shear-layer approximation, the only components of the stress tensor that are retained are those having gradients with respect to η only.

Turbulent heat transport is defined in terms of mean-energy gradients and an eddy-conductivity coefficient K_e such that $K_e = K + K_T$. Typically, the eddy-conductivity coefficient is related to the eddy-viscosity coefficient via a turbulent Prandtl number Pr_T where

$$Pr_T = C_p \mu_T / K_T$$

The turbulent Prandtl number is assumed constant at a value of 0.9.

The algebraic eddy-viscosity model used here is that proposed by Baldwin and Lomax.[10] This model is particularly well suited to complex flows that contain regions in which the length scales are not clearly defined. It is described briefly as follows: For wall-bounded shear layers, a two-layer formulation is used such that

$$\mu_T = (\mu_T)_{inner} \quad \text{for} \quad \eta < \eta_{crossover}$$

$$\mu_T = (\mu_T)_{outer} \quad \text{for} \quad \eta > \eta_{crossover}$$

where η is the normal distance from the wall and $\eta_{crossover}$ is the smallest value of η at which values from the inner and outer formulas are equal. The Prandtl-Van Driest formulation is used in the inner (or wall) region.

$$(\mu_T)_{inner} = \rho \ell^2 |\omega|$$

$$\ell = 0.4\eta\,[1 - exp(-\eta/A)]$$

$$A = 26\mu_w / \sqrt{\rho_w \tau_w}$$

The formulation for the outer region is given by

$$(\mu_T)_{outer} = 0.0168\, C_{cp} F_{wake} F_{Kleb}(\eta)$$

$$F_{wake} = \min\begin{pmatrix} \eta_{max} F_{max}, \\ C_{wk}\, \eta_{max}\, q_{dif}^2 / F_{max} \end{pmatrix}$$

The quantities η_{max} and F_{max} are determined from the function

$$F(\eta) = \eta\,|\omega|\,[1 - exp(-\eta/A)]$$

where F_{max} is the maximum value of $F(\eta)$, and η_{max} is the value of η at which it occurs. The function $F_{Kleb}(\eta)$

is the Klebanoff intermittency function given by

$$F_{Kleb}(\eta) = [1 + 5.5(C_{Kleb}\,\eta/\eta_{max})^6]^{-1}$$

The quantity q_{dif}^2 is the difference between the maximum and minimum total squared velocity in the profile (along an η-coordinate line),

$$q_{dif}^2 = q_{max}^2 - q_{min}^2$$

and for boundary layers, the *minimum* is defined as zero. The other constants are given by

$$C_{cp} = 1.6 \quad , \quad C_{wk} = 0.25 \quad , \quad C_{Kleb} = 0.3$$

The advantage of this model for boundary-layer flows are as follows: 1) for the inner region, the velocity and length scales are always well defined, and the model is consistent with the "law of the wall"; 2) in the outer region for well-behaved (simple) boundary layers, where there is a well-defined length scale (η_{max}), the velocity scale is determined by F_{max}, which is a length scale times a vorticity scale; 3) in the outer region of complex boundary layers where the length from a wall becomes meaningless, a new length scale is determined from a velocity (q_{dif}) divided by a velocity gradient ($|\omega|$), and the velocity scale is q_{dif}.

The outer formulation, which is independent of η, is also used in the free-shear flow regions of separated flow and in regions of strong viscous/inviscid interaction. In these regions the van Driest damping term, $[exp(-\eta/A)]$, is neglected. For jets and wakes, the Klebanoff intermittency factor is determined by measuring from the grid centerline, and the minimum term in q_{dif} is evaluated from the profile instead of being defined as zero.

The validity of the eddy-viscosity model constants for high-pressure, compressible exhaust jets has not been established, and compressibility effects are not accounted for.

At the exhaust-jet exit plane and in the near-base region, the eddy viscosity is assumed to be negligibly small and to increase spatially to the value given by the outer model over a short distance downstream of the base.

Computed Results

As mentioned in a preceding section (Afterbody Configuration), a flow field has been computed for the body placed at an angle of incidence of 6° to a free stream at Mach 2. The jet-exit Mach number is 2.5 with a static pressure 3 times that of the free stream. Beginning with an impulsive start in a uniformly flowing stream at Mach 2, the solution was advanced timewise to a dimensionless time ($t\,d/U_\infty$) of 5.1, where d is the forebody diameter and U_∞ is the undisturbed free-stream speed. Although a solution at a time of 5.1 is probably not sufficiently converged to permit valid quantitative comparisons with experiment, it is sufficient to establish the basic flow-field character and to illustrate the features of the solution and the computer code.

The initial time-step size of Δt =0.0001 was increased to Δt =0.001 as the solution passed through its initial rapid transient. A variable time-step was used in the subsonic flow regime downstream of the base in order to minimize the growth of nonlinear instabilities aggravated by changes in sign of the eigen-values in this region. The time-steps in this subsonic region were scaled down by a factor equal to the local streamwise Mach number with a cutoff minimum factor of 0.001 imposed to prevent the time-step from going to zero.

Occurring physically in this region is a rapid expansion of the jet around the nozzle lip followed immediately by a strong recompression in the form of a barrel shock; in addition there is a slip surface defining the boundary between the exhaust plume and the external flow. Each of these three high-gradient features is focused at the nozzle lip and demands a high degree of resolution that has not been provided for in the computational grid used here.

Shown in Fig. 5 are computed density contours in the bilateral plane of symmetry in the vicinity of the body. The lower surface is the wind side. Clearly defined downstream of the afterbody is the slip surface demarcating the boundary between the exhaust plume and the external flow. The propulsive jet expands rapidly around the nozzle lip and can induce low separation on the afterbody surface. For low-pressure jets, or no jet at all, there will be a region of recirculating flow on the blunt base. The afterbody drag is strongly influenced by the detail of the separated flow.

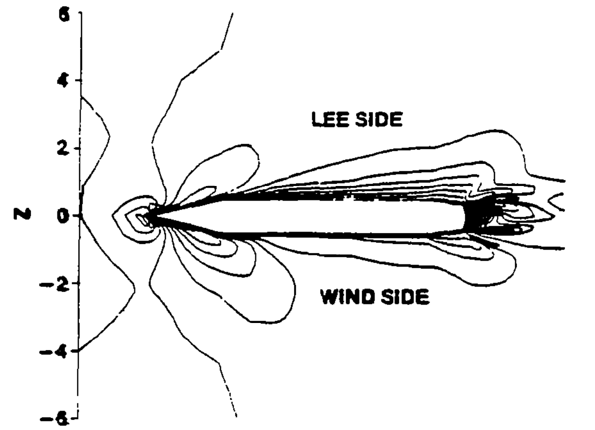

Fig. 5 Computed density contours, plane of symmetry: $M_\infty = 2$, $M_J = 2.5$, $P_J/P_\infty = 3$, $\alpha = 6°$, $Re_d = 1.5\text{x}10^6$.

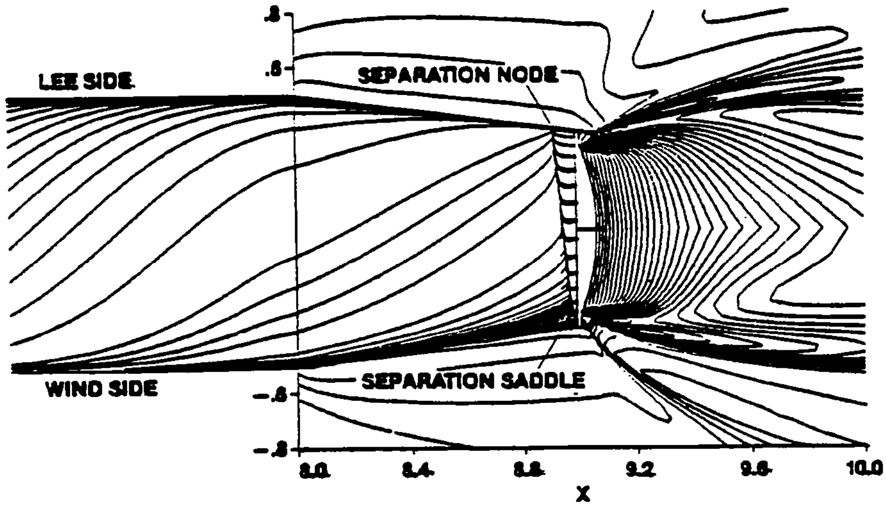

Fig. 6 Afterbody flow detail: surface streamlines and density contours on bilateral plane of symmetry.

The detail of the separation pattern is shown in Fig. 6 in which computed surface streamlines have been mapped on the afterbody and projected on the bilateral plane-of-symmetry view of the density contour plot over the aft portion of the body only. There is a separation node on the lee generator of the conical afterbody at $x = 8.92$. All surface streamlines on the lee side of the body flow into this node. A line of separation extends from this node, downward on the afterbody surface, to a separation saddle at $x = 8.98$, 33° from the wind generator. The flow direction along this line of separation is upward from the saddle to the node. There is also flow outward from the separation saddle downward to the end of the base, around to the wind generator.

Shown in Fig. 7 is a perspective view of the surface streamlines on the afterbody and the blunt base. The outer edge of the base is a dividing surface streamline extending from a saddle point on the lee generator to a node point approximately 33° from the wind generator. A dividing streamline can be seen circumscribing the annular base connecting a saddle point on the windward and a nodal point on the lee. This line separates the external flow from the flow from the jet. Flow is upward from the windward saddle to the lee-side node.

Shown in Fig. 8 is a sketch of an end-view projection of the full view of the afterbody (not to scale) showing all the dividing streamlines and their corresponding singular points and flow directions.

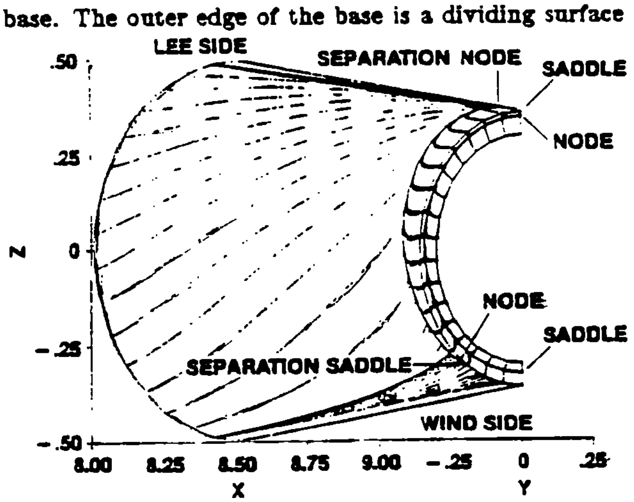

Fig. 7 Perspective view of surface streamlines over conical afterbody and annular base.

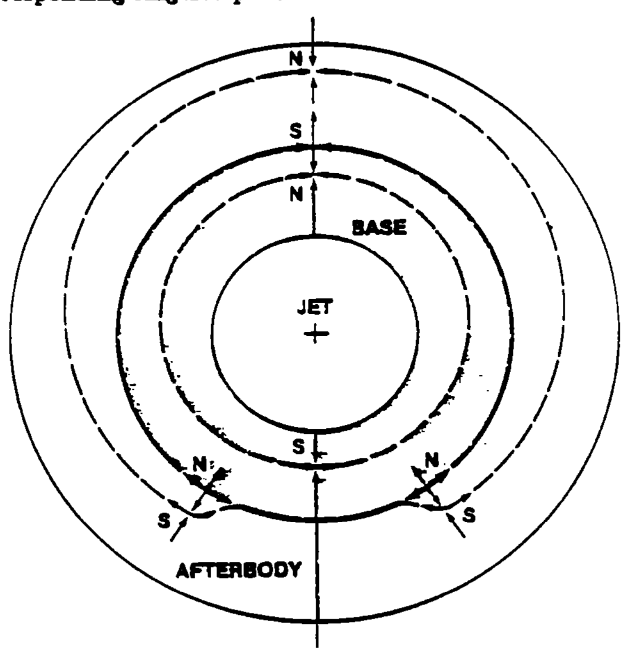

Fig. 8 End-view schematic of dividing surface and singular points streamlines.

The trajectories of the fluid particles in the plane of symmetry in the base region are shown in Fig. 9. On the lee, seen in Fig. 9a, the fluid from the jet expands around the nozzle lip and moves outward toward the edge of the base. Upon meeting the external flow, it turns downstream and defines the exhaust plume boundary. A region of reverse flow can be clearly seen above the afterbody lee generator. The path of the fluid in the external flow is over this separation region and around the afterbody base to the slip surface defining the boundary between the exhaust plume and external flow. The point defined by the outer edge of the base and the afterbody lee generator is a singular point that from the fluid streamlines, appears as a saddle point in both the circumferential plane and in the radial plane, and as a nodal point in the streamwise bilateral plane of symmetry (the plane of the base).

On the windward, shown in Fig. 9b, the streamlines just off the wind generator of the afterbody turn the corner and move toward the slip surface between the jet and the external flow. All external flow streamlines (excluding the surface streamline) approach the slip surface downstream of a saddle point in the bilateral plane of symmetry located at $x = 9.016$ on the plume-external flow boundary. The surface streamline turns the corner and approaches the windward saddle point on the base itself. Fluid from the jet expands around the nozzle lip and moves outward. The fluid just off the lip moves to the saddle point on the base and the fluid farther inside the lip expands toward the plume boundary downstream of the saddle point on the slip surface.

Surface-pressure distributions over the afterbody surface and over the base are shown in Figs. 10a and 10b, respectively. An expansion at the forebody-afterbody junction over the afterbody surface can be seen. This expansion is greatest on the windward, where the pressure level is highest, and decreases toward the lee. The circumferential variation of pressure near the lee side is quite small for the entire length of the afterbody. Toward the end of the afterbody there is a slight recompression on the lee side which is not observed on the windward. Just at the end of the afterbody there is an expansion as the flow turns around the afterbody toward the base.

Figure 10b shows a projected view of the base and jet-exit pressure distribution. The left side of the "top hat" pressure distribution corresponds to the lee, and the far side corresponds to the windward. The large uniform pressure distribution of the "top hat" configuration corresponds to the high-pressure jet, and the undulating "brim" of the hat is the distribution on the annular base. On the windward there is a rapid expansion at the nozzle lip followed by a fairly large recompression toward the outer edge of the base. The same trend is observed at other radial positions around the base but to a lesser degree. The circumferential variation of base pressure is consistent with the experimentally observed variation of White and Agrell for the same jet-to-free-stream pressure ratio. It is interesting to note, however, that in most experimental studies the radial variation of pressure is assumed negligible and is not measured. The distribution in Fig. 10b clearly indicates a substantial variation across the annular base.

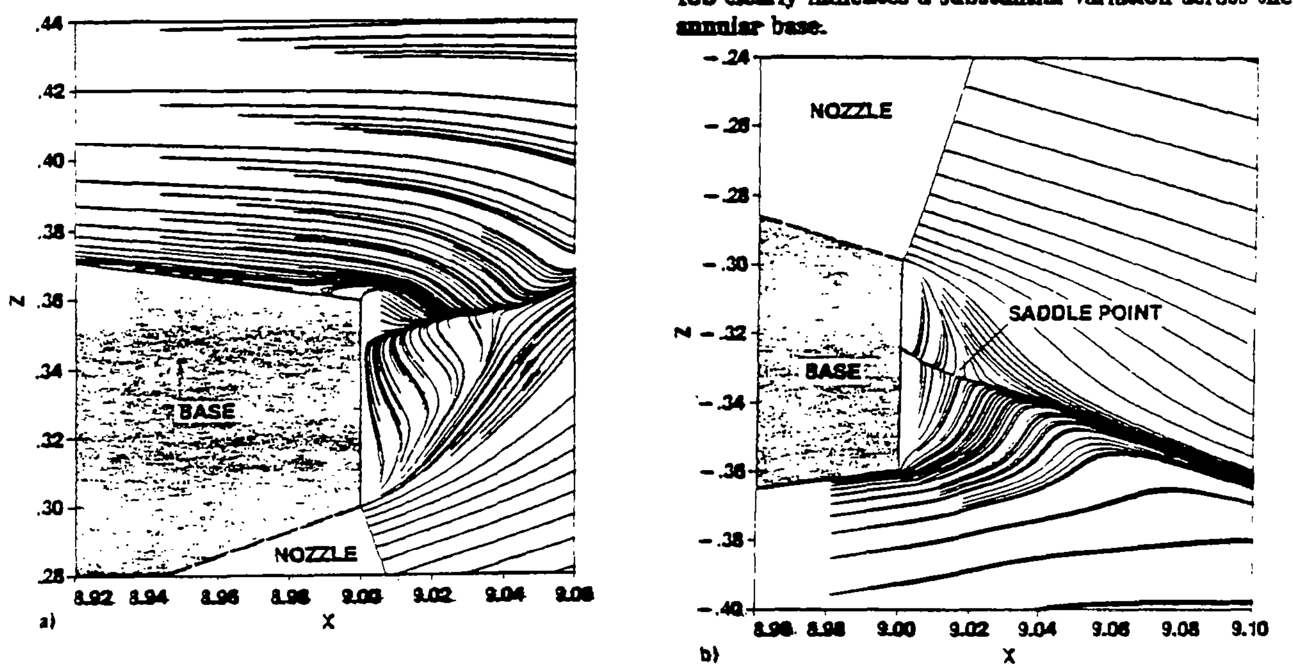

Fig. 9 Base-region path lines: plane of symmetry. a) Lee; b) Windward

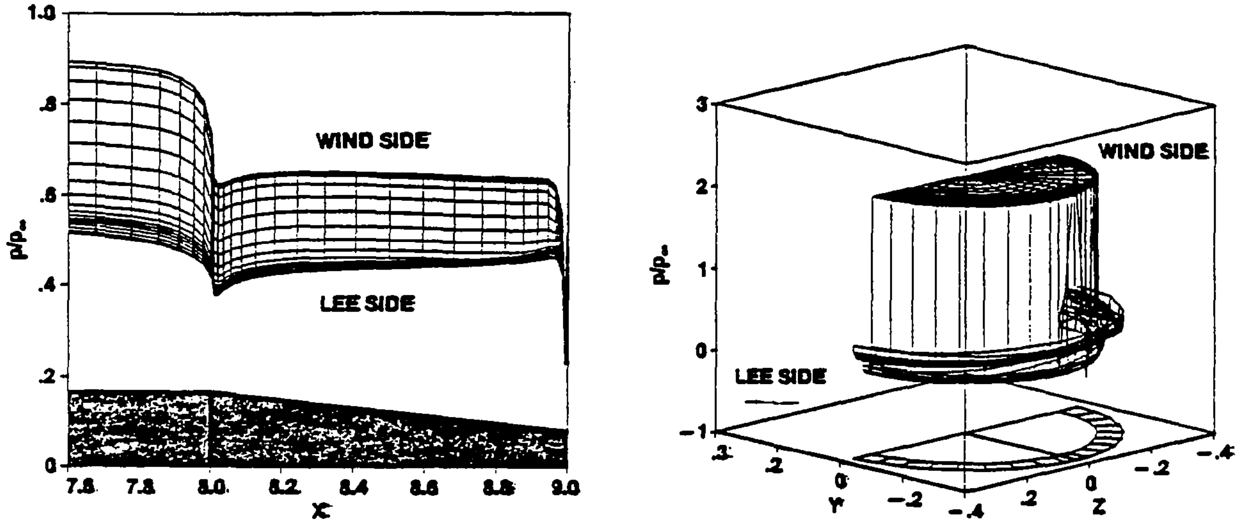

Fig. 10 Surface pressure distribution: perspective. a) Conical afterbody; b) Annular base and jet exit plane.

Concluding Remarks

An implicit solution procedure for the thin-layer approximation to the three-dimensional, time-dependent, compressible, Reynolds-averaged Navier-Stokes equations on a large array processor has been described. An example problem was simulated on the Cyber 205 computer that required a data base of 5×10^6 words. The efficient treatment of this large data base has been described in some detail.

The flow-field simulated was the supersonic flow over a body of revolution at incidence to the free stream. A propulsive jet emanated from the boattailed afterbody, inducing a complex, three-dimensional separated-flow pattern. This separated flow-field, which contributes substantially to the afterbody drag, has been described in detail for the particular geometry and flow conditions considered. The computed solution is consistent with experimental data observed for the same configuration and flow conditions.

References

[1]Deiwert, G. S., "Numerical Simulation of Three-Dimensional Boattail Afterbody Flowfields," AIAA Journal, Vol. 19, No 2, May, 1981, pp. 581-588.

[2]Deiwert, G. S., "A Computational Investigation of Supersonic Axisymmetric Flow over Boattails Containing a Centered Propulsive Jet," AIAA Paper 83-0462, 1983.

[3]White, R. A. and Agrell, J., "Boattail and Base Pressure Prediction Including Flow Separation for Afterbodies with a Centered Propulsive Jet and Supersonic External Flow at Small Angles of Attack," AIAA Paper 77-958, 1977.

[4]Vinokur, M., "On One-Dimensional Stretching Functions for Finite Difference Calculations," NASA CR-3313, 1980.

[5]Agrell, J. and White, R. A., "An Experimental Investigation of Supersonic Axisymmetric Flow over Boattails Containing a Centered Propulsive Jet," FFA Tech. Note AU-913, 1974.

[6]Lomax, H. and Pulliam, T. H., "A Fully Implicit Factored Code for Computing Three-Dimensional Flows on the ILLIAC IV," Parallel Computations, G. Rodrigue, Ed., Academic Press, New York, 1982, pp. 217-250.

[7]Beam, R. and Warming, R. F., "An Implicit Finite-Difference Algorithm for Hyperbolic Systems in Conservation-Law-Form," Journal of Computational Physics, Vol. 22, Sept. 1976, pp. 87-110.

[8]Pulliam, T. H. and Steger, J. L., "Implicit Finite-Difference Simulations of Three-Dimensional Compressible Flow," AIAA Journal, Vol. 18, No. 2, Feb. 1980, pp. 159-169.

[9]CDC Cyber 200 FORTRAN Version 2 Reference Manual, Control Data Corporation, Sunnyvale, Calif., 1981.

[10]Baldwin, B. S. and Lomax, H., "Thin Layer Approximation and Algebraic Model for Separated Turbulent Flows," AIAA Paper 78-257, 1978.